

# Conceptual design and preliminary characterization of serial array system of high-resolution MEMS accelerometers with embedded optical detection

Maximilian Perez<sup>†</sup> and Andrei Shkel<sup>‡</sup>

*Department of Mechanical and Aerospace Engineering, 4208 Engineering Gateway Building  
University of California, Irvine, Irvine, CA 92697-3975, U.S.A*

*(Received May 19, 2004, Accepted December 30, 2004)*

**Abstract.** This paper introduces a technology for robust and low maintenance cost sensor network capable to detect accelerations below a micro-g in a wide frequency bandwidth (above 1,000 Hz). Sensor networks with such performance are critical for navigation, seismology, acoustic sensing, and for the health monitoring of civil structures. The approach is based on the fabrication of an array of high sensitivity accelerometers, each utilizing Fabry-Perot cavity with wavelength-dependent reflectivity to allow embedded optical detection and serialization. The unique feature of the approach is that no local power source is required for each individual sensor. Instead one global light source is used, providing an input optical signal which propagates through an optical fiber network from sensor-to-sensor. The information from each sensor is embedded onto the transmitted light as an intrinsic wavelength division multiplexed signal. This optical “rainbow” of data is then assessed providing real-time sensing information from each sensor node in the network. This paper introduces the Fabry-Perot based accelerometer and examines its critical features, including the effects of imperfections and resolution estimates. It then presents serialization techniques for the creation of systems of arrayed sensors and examines the effects of serialization on sensor response. Finally, a fabrication process is proposed to create test structures for the critical components of the device, which are dynamically characterized.

## 1. Introduction

One of the most critical obstacles to the pervasive monitoring of highly distributed built and networked infrastructure is the true scalability of a sensor network system (Chong 1997, Aktan, Tsikos, Catbas, Grimmelsman and Barrish 1999). Scalability limitations can be further prescribed in terms of: power, size, cost, packaging, and communication. Fiber optic sensor networks are an attractive approach for the pervasive monitoring.

An important advantage of fiber optic sensors is their ability to provide passive sensing of a wide range of physical fields (Udd 1990). This not only means that the sensor head operates without the need for electrical power, but the overall system, including the input-output fibers which serve as the telemetry links, is also electrically passive, and thus the whole system exhibits a low intrinsic susceptibility to the effects of electromagnetic interference (EMI) and electromagnetic pulse (EMP).

---

<sup>†</sup>Doctoral Student, E-mail: perezma@uci.edu

<sup>‡</sup>Assistant Professor, Corresponding Author, E-mail: ashkel@uci.ed

There are many other advantages of the fiber optic sensors. Firstly, telemetry systems based on fiber optics are capable of carrying an enormous number of low-bandwidth sensor outputs; for example, 1000 sensors with a bandwidth requirement of 100 kHz require a transmission bandwidth of only ~100 MHz -relatively small compared to the bandwidths required for multi-gigabit data rate systems demonstrated in the optical fiber telecommunication field. Second, a single fiber or pair per servicing a large number of sensors provides a lightweight, low-cost telemetry link between the electro optics processing module and the sensor network or array, an advantage in applications where weight reduction is an important design consideration. Third, fiber optic links provide extreme versatility in configuring the telemetry system and network topology.

Several fiber optic based sensor systems have been attempted previously (Udd 1990). These prior attempts can be classified into three major categories: (1) Sensors based on Bragg gratings, (Yamakawa, Iwaki, Mita, and Takeda 1999, Todd, Johnson, Vohra, Chen-Chang, Danver, and Malsawma 1999, Gerges and Newson 1989b, Gerges and Newson 1989a), (2) Sensors based on Fabry-Perot interferometers, and (3) Sensors based on optical mode propagation effects. The third category is the least mature and doesn't appear to be extensible to multiple sensor arrays.

The most sensitive readout technique for fiber optic sensors is amplitude modulation by the "shoulder" of a narrow resonance peak (Stephensa 1993, Vohra, Danver, Tveten, and Dandridge 1997, Cooper and Post 2000). In this readout scheme, narrow-band illumination, typically from a laser, illuminates the shoulder of a rapidly varying transition in optical transmission. Mechanical effects that produce very small shifts in the position of the transmission curve produce large changes in the transmitted intensity.

Sensors based on Bragg gratings are suitable for integration into sensor arrays, but have significant limits on their sensitivity. The transduction mechanism for Bragg gratings is the mechanical stretching or compression of the length of the fiber containing the grating. While the width of optical resonance can be designed to be very steep, the glass from which the fiber is made has a very high Young's modulus (in a 100GPa range). This high stiffness is in conflict with high mechanical sensitivity. In operation, the resonant wavelengths of a Bragg grating are reflected and the remainder of the input spectrum transmitted. This property makes it possible to use Bragg sensors serially, provided each sensor in the sequence, each tuned to a sufficiently distinct wavelength. This is critically important if, as in the case for structural health monitoring, arrays of sensors are needed.

Another possibility for designing an optical sensor is to utilize a Fabry-Perot interferometer concept, (e.g. Choqueta and Juneau 2000). The transmission of a Fabry-Perot is the inverse of that of a Bragg grating; the resonant wavelengths are transmitted by a Fabry-Perot while those of a Bragg grating are reflected. This behavior prevents the serial use of Fabry-Perot and thus prevents them from being strung together to form an array. To illustrate, consider two serially connected Fabry-Perot sensor, each with a different resonant wavelength. The first would transmit only its resonant wavelength, so the second would not have any illumination in the spectral region of its resonance; it would have no light to modulate.

While the Fabry-Perot based sensors can achieve higher sensitivity than that of the Bragg-grating designs, they have several important drawbacks compared to the Bragg grating based designs, particularly when trying to use them in a multi-sensor array configuration. Despite the fact that Fabry-Perot based designs have the limitations described above, they do share the other important system advantages of the Bragg grating based designs that were described earlier: (i) neither electrical connections nor electronics are required in the sensor array and (ii) improved temporal bandwidth.

A number of suspended Fabry-Perot optical cavity devices have been developed in the past using

micro-fabrication techniques for various applications. Many have been based on integrated bulk micromachining processes due to the stable substrate available for optical deposition. A common technique is to use wet etching to create a cavity between the suspended and reference plates with a gold (Patterson 1997), aluminum (Cristea, Kusko, Tibeica, Muller, Manea, and Syvridis 2004), or other optical coating. Some have integrated photo-detectors onto the reference mirror to provide an electrical signal (Waters and Aklufi 2002). In some implementations, a micro-assembly of two components is used to form a device. This approach allows optical coatings of silver (Bartek, Correia, and Wolffenbuttel 1999) and dielectrics (Raley, Ciarlo, Koo, Trujillo, Yu, Loomis, and Chow 1992) to be applied to both inner surfaces of the Fabry-Perot cavity. Others have used surface micromachining techniques to create a suspended plate from dielectric optical surfaces. In this implementation, however, the induced in the dielectric surfaces residual stresses generally limit the device resolution (Winchester and Dell 2001). Common to all these devices is that none were able to achieve an high optical resolution due to mechanical defects or lack of an optical high quality surface on one or both surfaces of the cavity. Also common is that no device to date has been suitable for simple optical serialization for the construction of a distributable array.

In this paper, we introduce a new fiber optic seismic sensor based on a micro-electro mechanical (MEMS) Fabry-Perot interferometer. It has two major design innovations that enable this new design to overcome the limitations encountered previously in using Fabry-Perot structures for health monitoring sensor arrays: (1) simplified structure, implemented with MEMS technology, enables the fabrication of high finesse Fabry-Perot sensors that have one order of magnitude higher optical sensitivity than previous designs; and (2) A spectrally selective mirror design that enables multiple Fabry-Perot acceleration sensors to be serially concatenated in a simple way.

The proposed system is composed of a number of FPI-based single-axis accelerometers connected by an optical path, such as a flexible fiber-optic line. This optical path carries the acceleration information from each sensor to a signal processing unit, where the “real-time” acceleration values are made available to the end user. Since each accelerometer or sensor node can be placed spatially distinct from one another, the nodes can be distributed about a large-scale structure. Such a system is useful for any number of applications where distributed sensing is required.

This paper is organized as follows. Section II introduces the classical concept of a Fabry-Perot filter and explains how a basic structure of Fabry-Perot filter can be used as an optical accelerometer. This section also discusses the effect of non-idealities on performance of optical sensors and provide some useful guidelines for designing such systems. The concept of linear serialization of the Fabry-Perot interferometers is introduced in Section III. Section IV discusses the micro-fabrication process and sensor assembly. The paper concludes with an illustration of manufacturability of accelerometers utilizing highly compliant polymers as a mechanical suspension.

## **2. Fabry-perot interferometer based accelerometers**

### *2.1. FPI theory*

A parallel plate Fabry-Perot Interferometer (FPI) is a simple device consisting of two parallel partially-transmissive plates with highly reflective inner surfaces, whose principle of operation was conceived over a century ago (Fabry and Perot 1899). These surfaces form a resonant optical cavity of which only wavelengths that match the optical resonant condition can escape and pass through the

device (Fig. 1a), the operation of which is described extensively in the literature, (e.g. Macleod 2001, Born and Wolf 1999). These devices are often thought of as optical filters which remove components (wavelengths) of input light which do not satisfy the resonance condition and are used extensively as such in optical communication technology (Kartalopoulos 2000).

The theoretical transmittance of light of wavelength  $\lambda$  through an FPI is given by the Airy function:

$$T = \frac{T_s^2}{(1 - \mathcal{R}_s)^2} \left[ 1 + \frac{4\mathcal{R}_s}{(1 - \mathcal{R}_s)^2} \sin^2\left(\frac{2\pi\mu t}{\lambda}\right) \right]^{-1} \quad (1)$$

for normal incident irradiance, where  $T_s$  and  $\mathcal{R}_s$  are the transmittance and reflectance of the inner surface of the plates, respectively, and  $\mu$  is the index of refraction and  $t$  is the gap between the plates. Note that the *transmittance* ( $T$ ) is the ratio of transmitted to incident irradiance and, similarly, *reflectance* ( $\mathcal{R}$ ) is the ratio of reflected to incident irradiance, where irradiance has units [optical power/area]. In the absence of any absorption at the inner surface, the coefficient  $\frac{T_s^2}{(1 - \mathcal{R}_s)^2}$  approaches to one and  $T$  is unity at optical resonance. In any real device,  $T$  is also attenuated by losses in the bulk of the plate as well as by reflection and scattering at the outer surfaces, but these losses do not effect the shape of the Airy transmission given by Eq. (1).

The resonance condition relating the FPI gap width to the spectral placement of it's transmittance peak, or *fringe*, is given by

$$\mu t = \frac{n\lambda}{2} \quad (2)$$

where  $n$  is an integer known as the order of the FPI. Eq. (2) reduces to  $t = \frac{n\lambda}{2}$  in air ( $\mu_{air} \approx 1$ ). Commonly, MEMS-based FPI's use orders of  $n = 1$  due to micron-level plate spacing available in microsystems, but higher FPI orders maybe considered. This condition is meet at all values of  $n$ , and fringes appear throughout the FPI output spectrum (Fig. 1b).

A strong measure of the optical quality and usefulness of an FPI is the *finesse* ( $N$ ). The finesse is the

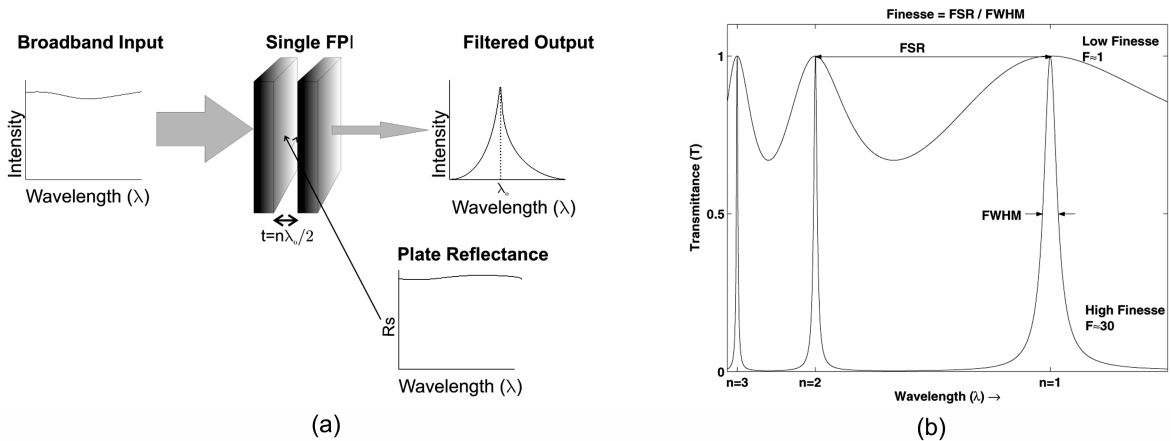


Fig. 1 (a) The operation of a single FPI about it's first order fringe and (b) The full characteristic transmittance pattern of an FPI

ratio of the separation of adjacent fringes (free spectral range or FSR) to the fringe width (full width of the fringe at half its maximum or FWHM). For an FPI without defects or optical absorption, the finesse is known as the *reflectance finesse* ( $N_R$ ), as it is related only to and increases monotonically with  $\mathcal{R}_s$ , and is given as

$$N_R = \frac{\pi\sqrt{\mathcal{R}_s}}{1 - \mathcal{R}_s} \quad (3)$$

Commonly, commercial FPIs have finesse values of  $N \approx 50-100$ , but some tunable telecommunication FPIs have achieved finesse values up to 2000 (Solus-Micro-Technologies 2002). In order to achieve a high finesse device, both high reflectivities and fine control over plate defects and parallelism must be obtained, as will be discussed.

The FWHM is the principle measure of the narrowness of the fringe and is important for determining the resolving power of an FPI. The FWHM of a defectless FPI fringe is given by

$$\delta\lambda_R = \frac{\lambda(1 - \mathcal{R}_s)}{n\pi\sqrt{\mathcal{R}_s}} \approx \frac{\lambda_c(1 - \mathcal{R}_s)}{n\pi\sqrt{\mathcal{R}_s}} \quad (4)$$

where  $\lambda_c$  is the wavelength at the center of the spectral region of interest.

The FSR is a measure of the spectral spacing between adjacent fringes. It is calculated as

$$FSR = \frac{\lambda}{n} \approx \frac{\lambda_c}{n} \quad (5)$$

and is important for determining the usable spectral range for an FPI.

## 2.2. FPI as an acceleration sensor

If one plate of an FPI is deflected relative to the other and the gap between the plates is changed (Fig. 2a), the resonant condition of the FPI changes and the transmitted fringe relative to wavelength shifts (Fig. 2b). By suspending one plate relative to the other (on a suspension of stiffness  $k$ ), the suspended plate acts as a proof mass  $m$  (Fig. 2c). The proof mass will respond to an acceleration of the plate fixed

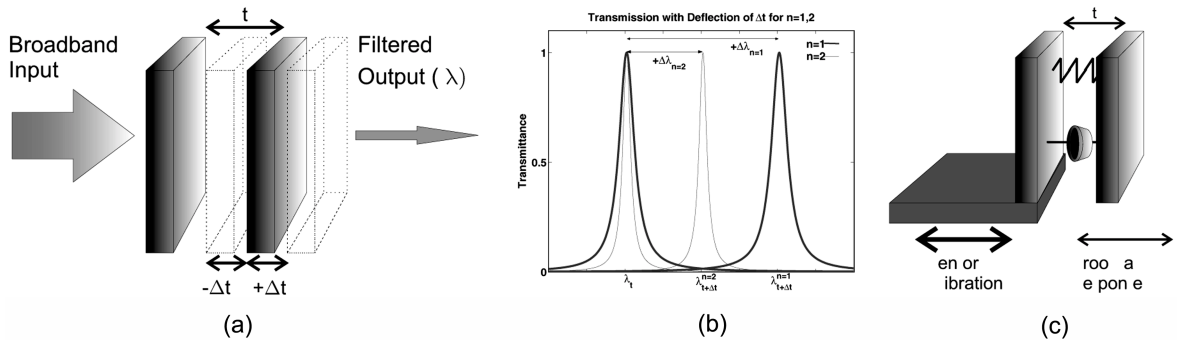


Fig. 2 (a) FPI with different spacing between reflective surfaces, (b) Shift of transmission curve of a single FPI due to changes in spacing between two mirrors. Two FPI orders are considered (with  $n=1$  and  $n=2$ ), and (c) Mechanical, lumped mass-spring-damper model, of an FPI-based sensors

to a structure of interest with a relative deflection  $\Delta t$  of the proof mass. Thus, by monitoring the spectral output of such an FPI, structural acceleration can be determined.

This response is simply governed by the difference version of the optical resonance condition, Eq. (2), given by

$$\Delta t = \frac{t}{\lambda} \Delta \lambda \quad (6)$$

where  $t$  is the plate gap and  $\lambda$  is the resonant wavelength of interest. Combining Eq. (6) with the expression for the optical resonance condition in air, Eq. (2), we obtain the spectral response of an FPI to deflection  $\Delta t$

$$\frac{\Delta \lambda}{\Delta t} = \frac{2}{n} \quad (7)$$

This ratio is constant for any system of order  $n$ . Note that as the order increases, the fringe spectral response is proportionally slower to relative deflections in the FPI plates.

The static response of a such a suspended mass is defined by combining Newton's 2nd Law and Hook's Law yielding

$$a = -\frac{k}{m} \Delta t = -\omega_n^2 \Delta t \quad (8)$$

This is the quasi-static relation for the deflection of a suspended plate  $\Delta t$  from rest due to an acceleration, where  $\omega_n$  is the angular natural frequency of the system. This relationship is generally true while the angular frequency of the acceleration is less then half of the natural frequency of the system ( $\omega < \frac{1}{2} \omega_n$ ), which also roughly accounts for the frequency bandwidth of such a system ( $\Delta f \approx 0 \rightarrow \frac{1}{2} \frac{\omega_n}{2\pi} \text{ Hz}$ ).

By combining the optical response, Eq. (7), with the mechanical response, Eq. (8), we obtain

$$a = \frac{-\omega_n^2 n \Delta \lambda}{2} = \frac{-\omega_n^2 n (\lambda - \lambda_o)}{2} \quad (9)$$

This is the governing relationship between the FPI sensor signal and it's experienced acceleration. Since  $\omega_n$  and  $n$  are sensor characteristics, Eq. (9) indicates that the change in peak transmitted wavelength  $\Delta \lambda$  determines the structure acceleration. In the simplest case, the device monitoring the wavelength of the peak transmission yields a functional optical accelerometer.

We can consider the FWHM  $\delta \lambda_R$  to be the coarse optical resolution of each FPI sensor and set it equal to  $\Delta \lambda$  to find the upper limit of the acceleration resolution  $\delta a$ . Doing this and combining Eq. (9) and Eq. (7) yields

$$\delta a = \frac{\omega_n^2 \lambda}{2} \frac{1 - \mathcal{R}_s}{\pi \sqrt{\mathcal{R}_s}} \approx \frac{\omega_n^2 \lambda_o}{2 N_R} \quad (10)$$

were we replace  $\lambda$  with  $\lambda_o$  to indicate that the calculation is done at the resonant wavelength when the system is at rest. It is important to note that although the FWHM narrows for higher order (larger  $n$  value) devices, the slower spectral response of the fringe causes the acceleration resolution to be independent of the FPI order. Eq. (2) and Eq. (8) can be combined to estimate the maximum of acceleration.

$$a_{\max} = \frac{\omega_n^2 n \lambda_o}{2} \quad (11)$$

If accelerations are below this value, the condition guarantees to prevent contact between the plates that would cause signal saturation.

If we assume that our FPI sensor is constrained for use in specific regions of the optical spectrum (for reasons such as the characteristics of the optical source, transmission system, detector or the spectral characteristics of the FPI's plates) constituting our *optical bandwidth* or  $\Delta\lambda_R$ , our acceleration range is limited to deflections corresponding to that region. If we assume that the rest resonant frequency  $\lambda_o$  occurs at the center of this region  $\lambda_c$ , from Eq. (9) we obtain the range of each sensor to be

$$\Delta a = \omega_n^2 n \Delta\lambda_R \quad (12)$$

since  $\Delta\lambda_R$  is symmetric about the rest frequency.

Finally, using Eq. (10), Eq. (12), and Eq. (5) we can introduce a quantity of merit that is the dynamic equivalent of the optical finesse and will be called the acceleration finesse of the system ( $N_a$ ).

$$N_a = \frac{\Delta a}{\delta a} = \frac{2N_R n \Delta\lambda_R}{\lambda_o} = \frac{2N_R \Delta\lambda_R}{FSR} \quad (13)$$

This quantity measures the ratio of the acceleration range to the acceleration resolution. Note that this quantity increases with the three characteristic optical quantities ( $N_R$ ,  $n$ ,  $\Delta\lambda_R$ ), but is not dependent on the mechanical characteristics,  $\omega_n$ , of the sensor. However, we observe that by increasing  $n$ , the free spectral range of the FPI decreases. If the  $FSR < \Delta\lambda_R$ , then we will observe multiple fringes in the optical bandwidth. To prevent this, we set  $\frac{\Delta\lambda_R}{FSR} = 1$  and find

$$N_{a,\max} = 2N_R \quad (14)$$

which is the maximum acceleration finesse obtainable with an FPI based accelerometer with a fixed optical bandwidth. This is equivalent to maximum number of discrete accelerations the FPI sensor can detect.

The simple sensor system proposed here depends heavily on two parameters: in the mechanical domain the sensitivity depends on the natural frequency of the suspended system, while in the optical domain the sensitivity depends on the interferometer finesse. The relations governing the operation of the FPI-based accelerometer scale with the square of the system natural frequency. Another important design parameter to consider is the frequency separation between the desirable, primary mode (typically, the first fundamental mode), and secondary, undesirable mode. In our device, the primary mode is the linear out-of-plane displacement mode and an undesirable mode -the torsional mode. As such, determination of the fundamental natural frequency of the suspended plate is important as well eliminating coupling to higher order modes. From the optical design point of view, both the acceleration resolution, Eq. (10), and maximum acceleration finesse, Eq. (14), have been shown to improve with the reflectance finesses ( $N_R$ ) demonstrating the critical nature of optical quality of such a system. For any real system, the reflectance finesse is not achievable and is replaced with the measured optical quality of the system ( $N$ ) or can be estimated by accounting for defects and calculating the effective finesse ( $N_{eff}$ ).

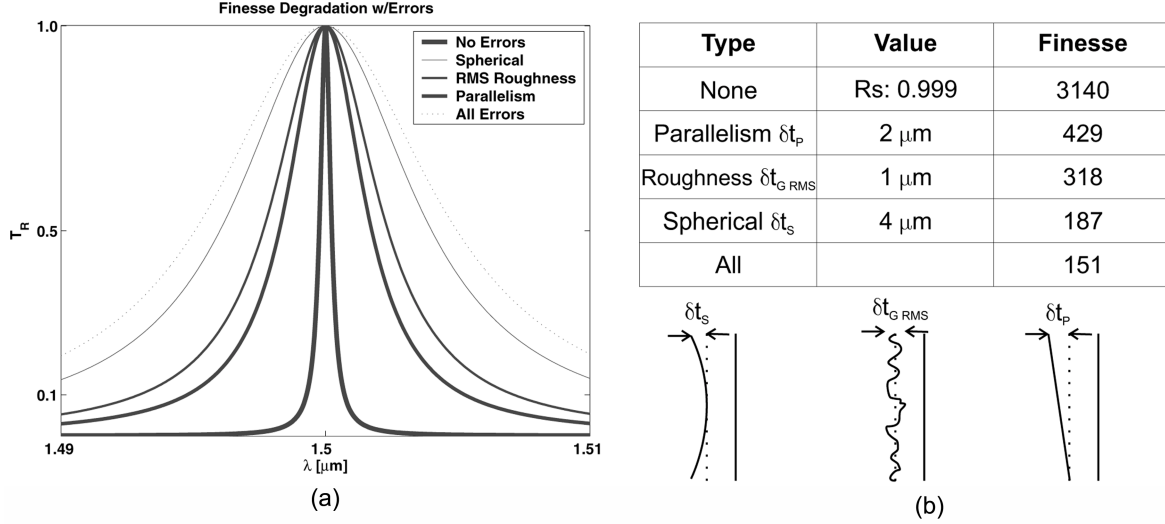


Fig. 3 (a) The transmission fringe of an high reflectivity ( $\mathcal{R}_s$ : 0.999) FPI with and without defects and (b) On the top, the corresponding defect type and finesse values for a system of 2 mm radius plates. Note, higher finesse values correspond to a narrower fringe

### 2.3. Effective finesse and imperfections in FPIs

The finesse of an actual device is limited by departures from the ideal parallel plate Fabry-Perot system, such as is due to defects in the plates, and can be calculated as the *effective finesse* or  $N_{eff}$ . Specifically, the  $N_{eff}$  decreases with increases in plate *spherical bowing*, plate *roughness*, and departures from *parallelism* between the two plates and is calculated from the maximum linear deviations from ideal due to each defect ( $\delta t_s$ ,  $\delta t_{G\text{ RMS}}$ , and  $\delta t_p$ , respectively). Fig. 3 demonstrates the dramatic decrease in finesse experienced by a high reflectivity system in the presence of mechanical errors, showing a three order of magnitude decrease in finesse in the presence of all error types.

Following Atherton (Atherton, Reay, Ring, and Hicks 1981), effective defect finesse can be calculated for each defect type as

$$N_S = \frac{\lambda}{2\delta t_s} \quad N_{G\text{ RMS}} = \frac{\lambda}{4.7\delta t_{G\text{ RMS}}} \quad N_P = \frac{\lambda}{\sqrt{3}\delta t_p} \quad (15)$$

for spherical bowing, surface roughness, and departures from parallelism, respectively.

The maximum deviations due to these errors ( $\delta t_s$ ,  $\delta t_{G\text{ RMS}}$ ,  $\delta t_p$ , respectively) can be calculated from simple geometry. The effective defect finesse due to all errors is calculated as

$$\frac{1}{N_D^2} = \frac{1}{N_S^2} + \frac{1}{N_{G\text{ RMS}}^2} + \frac{1}{N_P^2} \quad (16)$$

and this contributes to the total effective finesse ( $N_{eff}$ ) of the system by

$$\frac{1}{N_{eff}^2} = \frac{1}{N_D^2} + \frac{1}{N_R^2} \quad (17)$$

In these estimations, we have ignored finite aperture effects and assumed the incident light is perfectly collimated. Eq. (17) shows that in the case of high reflectance systems, where  $N_R \gg N_D$ , the effective finesse  $N_{eff} \approx N_D$ , and the system is dominated by mechanical errors.

In the development of a system as it is proposed here, all quantities of merit (such as acceleration resolution and acceleration finesse) can be improved by increasing the reflectance of the system. However, the cost of producing high reflectance plates is often dominated by the high cost of the deposition of additional high quality optical thin films. In order to ensure that the actual finesse ( $N_{eff}$ ) is of the order achievable by the  $\mathcal{R}_s$  to which the system has been designed, we can set limits on the FPI non-idealities introduced by errors mentioned above.

For instance, by assuming that the individual mechanical error finessses are equal to the theoretical reflectance finesse ( $N_R = N_S = N_{G,RMS} = N_P$ ) and using Eq. (16) and Eq. (17), we find that our effective finesse is  $N_{eff} = \frac{N_R}{2}$ . This allows us to ensure that if the error deviations ( $\delta t_s, \delta t_p, \delta t_{G,RMS}$ ) are less than the limits set by their respective error finessses according to relations of Eq. (15), then the finesse of an ideal interferometer  $N_R$  (estimated from the  $\mathcal{R}_s$ ) will be of the order of the effective finesse  $N_{eff}$ , such that  $N_R \geq N_{eff} \geq \frac{N_R}{2}$ . Without this analysis, any sensitivity gains from developing higher  $\mathcal{R}_s$  reflectors will be lost due to the mechanical tolerances and errors. Although looser mechanical tolerances are possible with higher reflectivity devices to achieve identical  $N_{eff}$ , and vice-versa, the above equality between defect and reflectance finessses represents a reasonable trade-off between the two competing features of creating a high actual finesse FPI.

For use in design, the maximum linear deviation due to the individual errors are plotted against the theoretical finesse and design reflectance assuming the equality of all finesse values associated with corresponding defects (Fig. 4). This allows one to set the error values for possible  $\mathcal{R}_s$  design values. For instance, in an example system where the minimum  $\mathcal{R}_s$  allowed in the optical bandwidth is 0.97, the

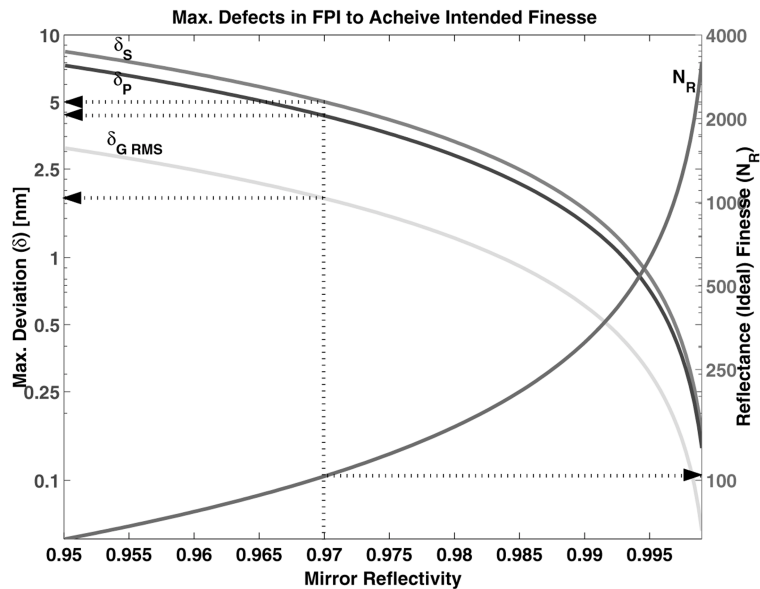


Fig. 4 The maximum linear deviation from an ideal system that an FPI can sustain due to spherical bowing ( $\delta_s$ ), parallelism deviation ( $\delta_p$ ), and roughness ( $\delta_{G,RMS}$ ), while still maintaining  $N_{eff} \geq \frac{N_R}{2}$ . Note system assumed to 2 operate at  $\lambda \approx 1550$  nm

limits on the maximum deviations from ideal are on the order of  $\sim 2\text{-}5$  nm in order to insure  $N_{eff} \geq \frac{N_R}{2} \approx \frac{100}{2} \approx 50$ . For use as an accelerometer, this means we must be certain that example system will not deviate from parallel motion by more than  $\sim 5$  nm in our expected inertial environment, as well as be sure that our fabrication process does not allow an root-mean-square (RMS) surface roughness or spherical bowing deviation greater than  $\sim 2$  nm or  $\sim 4.5$  nm, respectively. Fig. 4 also demonstrates clearly how the mechanical tolerances should be tightened as the design reflectance is increased in order to prevent the excess loss of finesse through the increased cost of FPI reflective plates.

#### 2.4. FPI sensor performance

Although, the coarse acceleration resolution and resolution trends of an FPI accelerometer are given by (10), the actual resolution depends on the system architecture and signal detection techniques. Here we examine two simple methods to determine the resolution limits of an FPI accelerometer. The conceptually simplest method of fringe peak detection ( $\lambda$ ) is the use of a broadband light source and an Optical Spectrum Analyzer (OSA) at the beginning and end of the optical path, respectively. The light source provides a broad-band signal for the network. An OSA sweeps a wavelength range and detects the spectral intensity of a signal and this architecture would yield an output similar to Fig. 2b. It is assumed then that the resolution is limited by the OSA's spectral resolution. For example, use of an Agilent 86144B with a wavelength resolution of  $\Delta\lambda = \pm 0.01$  nm in 1480 nm-1570 nm would yield (from Eq. (9)).

$$\delta a = \frac{(2\pi 2000 \text{ Hz})^2 (1)(0.01 \text{ nm})}{2g} = 80.5 \mu\text{g} \quad (18)$$

for a system having a frequency bandwidth of 1000 Hz and FPI order  $n = 1$ . OSA's have the advantage of being pre-configured for the detection of intensity peaks and for determining peak drift ( $\lambda - \lambda_0$ ) over time, as required by Eq. (9). However, the maximum scan rate of such an OSA is less than 20 Hz unacceptably limiting the frequency bandwidth.

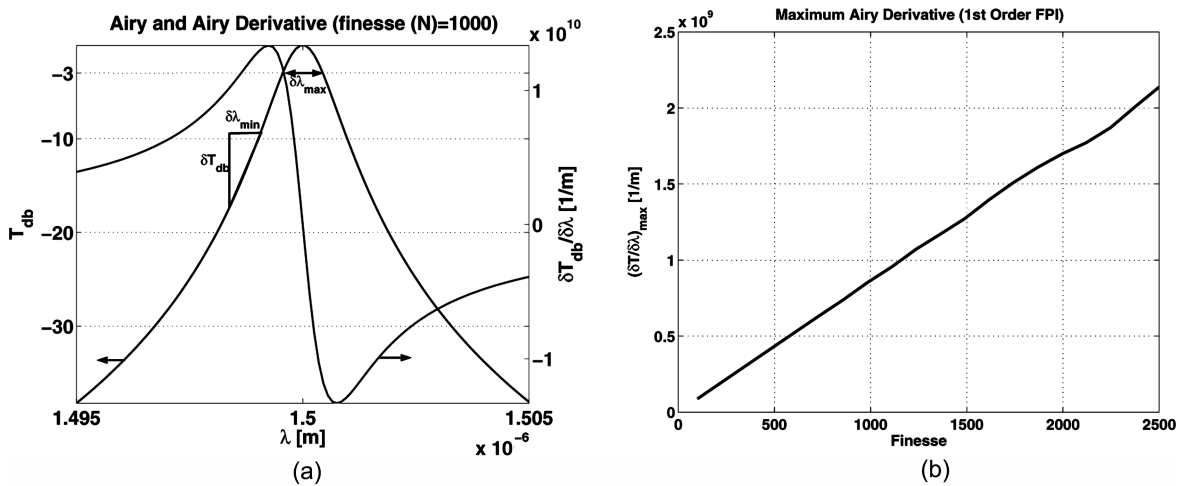


Fig. 5 (a) The Airy function and its derivative for a 1000 finesse FPI and (b) The variation of Airy slope with finesse

In order to improve the range of frequency use to the full range of the sensor design, a laser-line source could be used with a photodetector. Now the intensity experienced at the detector is simply the optical power times the transmittance of the Airy fringe at the laser wavelength. If the rest wavelength of the FPI is set such that the laser wavelength falls between the -3 db and -10 db points of the Airy fringe where the slope of the Airy function is a maximum (Fig. 5a), any deflection of the fringe will cause the transmittance at the laser wavelength to change. This corresponds to a shift in the output optical intensity that is detected by the photodetector and output as a voltage. The maximum spectral resolution of such a system is given by

$$\delta\lambda_{\min} = \frac{\delta\lambda}{\delta I} \frac{\delta I}{\delta V} \delta V \quad (19)$$

where  $\frac{\delta I}{\delta V}$  is the sensitivity of the photodetector,  $\delta V$  is the resolution of the voltmeter, and  $\frac{\delta\lambda}{\delta I}$  is the same as inverse slope of the (Airy) intensity curve, which is a strong function of FPI finesse (Fig. 5b). A 1500 nm laser directed through a FPI of finesse  $N=1000$  ( $\frac{\delta\lambda}{\delta I} \approx 1 \times 10^{-10}$  m) to a ThorLabs PDA255 photodetector ( $\frac{\delta I}{\delta V} \approx 1$  W/V) coupled to a standard voltmeter ( $\delta V \approx 1 \times 10^{-3}$  V), yields  $\delta\lambda_{\min} = 1 \times 10^{-4}$  nm. Again, the acceleration resolution is found using Eq. (9), resulting in

$$\delta a = \frac{(2\pi 2000 \text{ Hz})^2 (1)(1 \times 10^{-4} \text{ nm})}{2g} = 0.8 \mu g \quad (20)$$

This illustrates the capabilities of an FPI-based optical accelerometer. It should be noted however that this is the highest achievable resolution from the Airy curve and the use of this technique over a wider bandwidth would result in poorer resolutions. By extending the range to operate along the Airy curve from -3 db to -30 db, we expect the resolution to increase by a factor of two due to the variation in the Airy slope.

### 3. FPI serialization and system design

Generally, FPI sensors cannot be used in simple series with the output of one sensor providing the input of the next. This is due to fact that the FPI is a rather effective optical filter and upstream devices “use” wavelength components that downstream devices need to produce optical resonant fringes. While serial arrays of “solid etalon” (fixed cavity) FPIs have been used in the communications industry for years to provide high finesse optical filters (Macleod 2001), this technique is not adequate for sensing since it results in the fringes from the individual FPIs fall on top of each other (spectrally) to improve finesse by iteratively sharpening the fringe peak. In general, if the resonant condition of any of the FPIs in a series deviates from each other by more then the width of the fringe, then all fringes disappear at the output of the series (Fig. 6).

However, if the plates of the FPIs are made using high quality *notch* reflectance mirrors, they will be reflective only in a small segment of the spectrum. Light will be filtered only in that notch region of the spectrum, creating an Airy fringe signal, and will leave the rest of the light to pass on to downstream devices. Each of these downstream devices in turn have their notches in a different spectral region and produce their own fringe signal distinct from the upstream devices. The series of notch reflectance FPI's now acts as an intrinsic coarse wavelength division multiplexing network with the acceleration

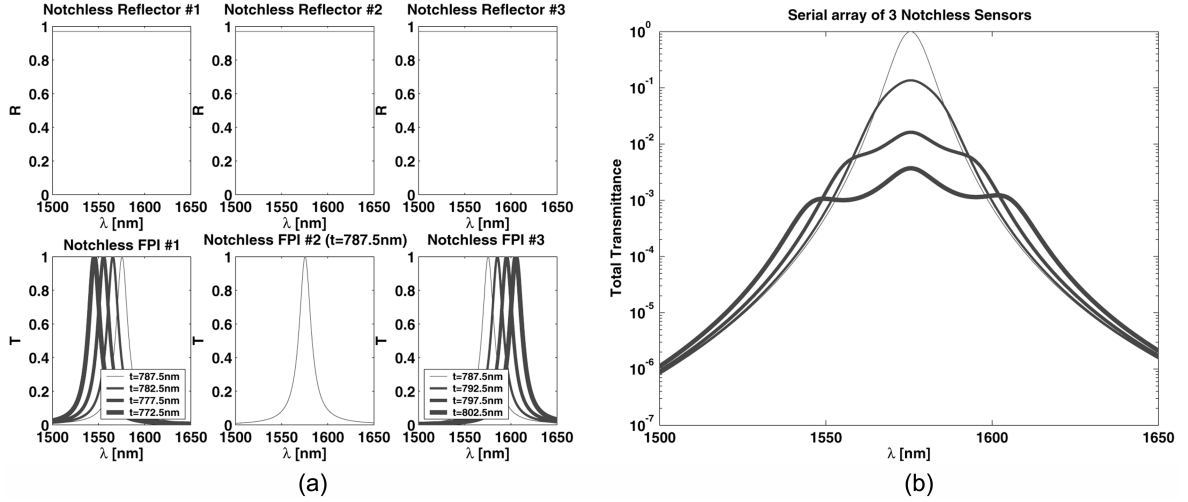


Fig. 6 A (simulated) serialized system of three FPI sensors without notched reflectance characteristics where (a) On the top, the reflectance characteristics of the sensor plates, and at the bottom, the transmittance signal through each sensor for a variety of plate spacings, and (b) The total transmittance signal through the system. Note that only when the individual transmittance signals overlap spectrally due to each sensor having identical plate spacing does a signal propagate through the system

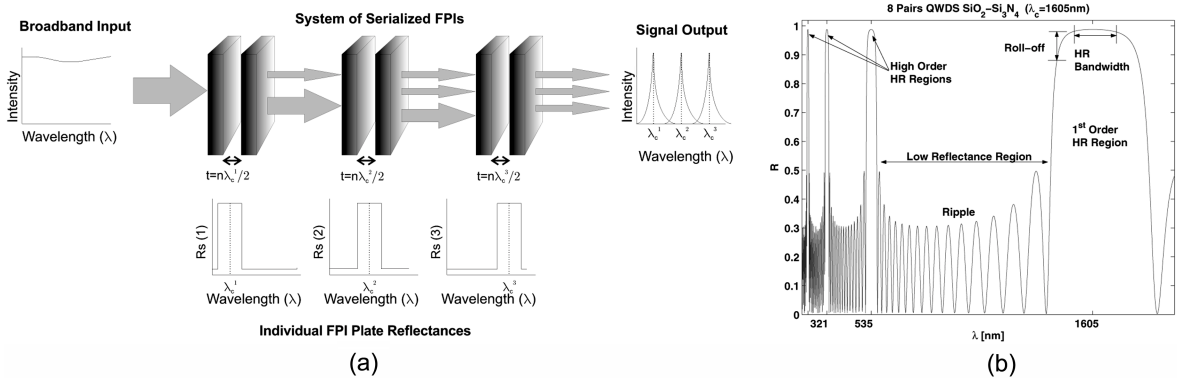


Fig. 7 (a) The operation of a series of FPIs with notch reflection characteristics and (b) A realizable notch reflectance pattern with non-ideal characteristic.

signals embedded onto each channel of the input signal (Fig. 7a). If one could observe the light coming from the end of such a system in a visible broadband light spectrum, one would see a rainbow of light with one pure color for each sensor. Accordingly, each color would be rapidly changing according the acceleration experienced by it's sensor node.

The mechanical characteristics of each sensor of such a system are designed such that each FPI sensor operates only in the optical bandwidth defined by it's notch or high-reflectance (HR) zone, such that  $\Delta\lambda_R = \Delta\lambda_{HR}$ . This will produce an Airy fringe for each sensor at the output signal. One of the difficulties of such a system is that perfect notch reflectors having  $\mathcal{R}_s = \mathcal{R}_{max}$  throughout the optical bandwidth and  $\mathcal{R}_s = \mathcal{R}_{pass} = 0$  elsewhere are impossible to produce in practice and a reflectance pattern similar to Fig. 7b is produced instead. The effects of this phenomenon are studied below.

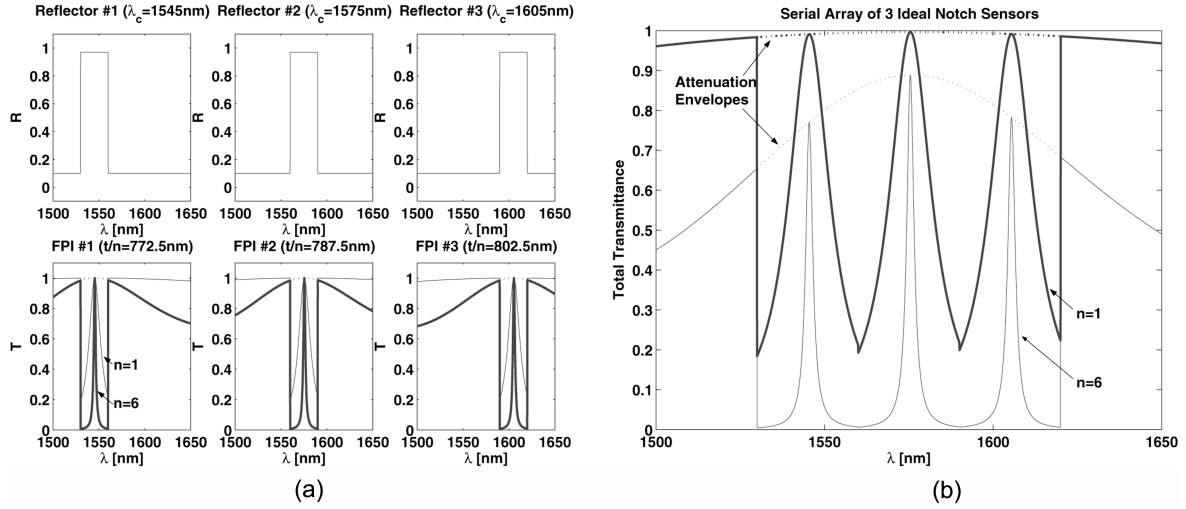


Fig. 8 Numerical simulation of a series array of three FPI sensors of  $R_{\max} = 0.97$  and  $R_{\text{pass}} = 0:1$  with (a) On the top, the individual reflectance characteristics, and at the bottom, the transmittance characteristics and (b) The system transmittance signal for  $n=1, 6$ . The dotted line represents the transmission attenuation envelope

### 3.1. Ideal serialized sensor system

In the following we design and simulate a system of three sensors to explore the effects of serial-ization. The first step in developing the optics of a system such as proposed here is deciding the optical range in which to work. We propose using the optical communication  $C+L$  band (1528-1620 nm) due to wide selection of equipment available (optical sources, fiber, and detectors) for use in this range. Another reason for selecting this band is to utilize  $S_i$  micro-fabrication technology, and  $S_i$  is highly transparent to these wavelengths (Kartalopoulos 2000, Goff 1999). We choose our optical bandwidth such that our chosen optical range is saturated with non-overlapping notch reflectance regions, one for each sensor. Thus, in the case of the  $C+L$  band with three sensors,  $\Delta\lambda_R \approx 30$  nm.

Such a system can be simulated by calculating the transmittance of each FPI and of the entire system. For each wavelength of interest, a reflectance is defined. In the case of the ideal notch reflector, the reflectance is either  $R_{\max}$  within the notch or  $R_{\text{pass}}$  outside it. Using the Airy function, Eq. (1), the transmittance of each FPI sensor is calculated at each wavelength. The transmission signal of the system is simply the product of all the individual transmittances through each sensor and the transmission of the source ( $T_{\text{system}}(\lambda) = T_{\text{source}}(\lambda) \times T_1(\lambda) \times T_2(\lambda) \times T_3(\lambda) \times \dots$ ) calculated at each wavelength. Here we calculate the  $T_1(\lambda) \times T_2(\lambda) \times T_3(\lambda) \times \dots$  system transmittance terms only, leaving the system source undetermined until the final detection architecture is decided.

Such a system is shown in Fig. 8 for two system of series of three FPI sensors of different orders. We note that the severe signal attenuation and distortion of the individual signals of the notchless system of Fig. 6 is not observed and the individual fringes are readily apparent in the series signal. However, since the reflectance outside the notches is nonzero, attenuation still occurs. Furthermore, this attenuation is determined by the composite Airy function transmission ( $T_1 \times T_2 \times T_3 \times \dots$ ) of the system calculated using  $R_{\text{pass}}$  and so has an effect greater than the simple sum of the blocking due to  $R_{\text{pass}} \neq 0$ , as might be expected. We will call this effect the attenuation envelope. We note that no individual FPI signal exceeds the attenuation envelope and that, except for the slight effects due to the shape of the envelope,

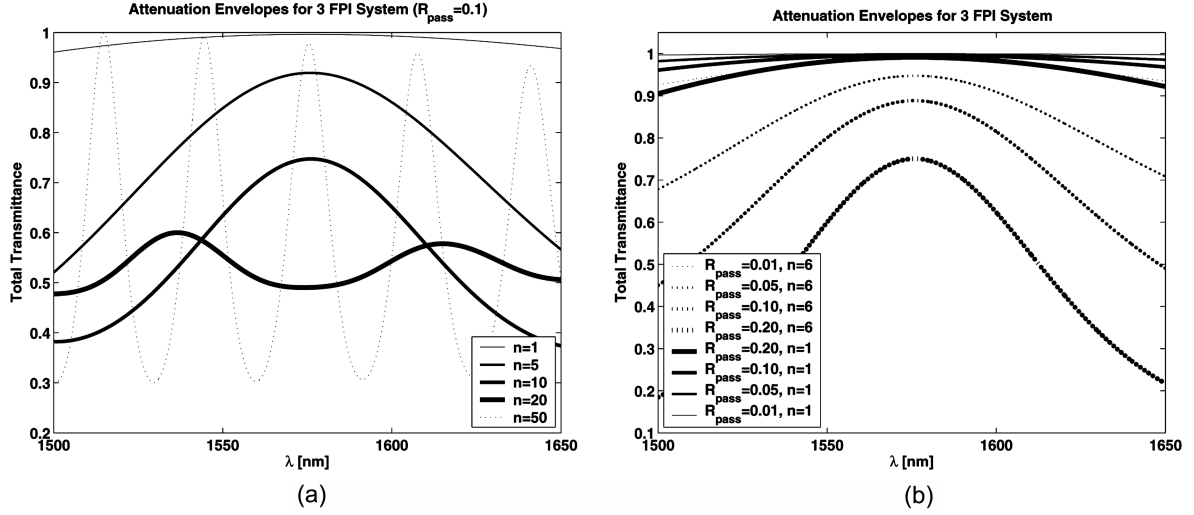


Fig. 9 The effect of (a) FPI order and (b)  $R_{pass}$  on the attenuation envelope

these signals are simply attenuated and not deformed. The effects of the attenuation envelope are further complicated by the fact that its shape shifts with the deflection of any of the sensors due to the change in optical resonance condition and the change in the Airy transmission of that sensor element.

We note from Eq. (13) the maximum acceleration .esse can be achieved by setting  $FSR = \Delta\lambda_r$ . Since our choice of range implies  $\lambda_c \approx 1575$  nm, it can be concluded that our most efficient order is  $n \approx 52$ . However, Fig. 9a shows that as the period of the Airy function grows shorter as the order is increased, the attenuation envelope grows more complicated and the attenuation effects are increased. For example, for system of 1st order devices with  $R_{pass}=0.1$ , the attenuation due to this effect is less than 5% across the entire optical region of operation, whereas for a system of  $n=50$  the individual signals may be attenuated by up to 70%. This would imply for systems in which a constant amplitude signal response is desired, such as the first detection architecture discussed in section II-D, serialized systems of this type must be composed of low order FPI sensors. For the higher resolution second detection method discussed in section II-D, this complex attenuation would be devastating and low order systems are required.

In addition, Fig. 9b shows how the effects of the attenuation envelope increases dramatically with the increase in  $R_{pass}$ . Although minimizing  $R_{pass}$  is preferable in any case, some residual  $R_{pass}$  is expected in any real reflector and may be substantial for further encouraging the use of low order FPIs in serialized systems.

### 3.2. On mirror design

Sophisticated optical processing must be performed to create the reflectors used in high-performance FPIs to achieve the high reflectivities required for precision detecting. This is usually achieved by depositing alternating layers of high and low index of refraction dielectric material in optical thin films on a transparent substrate, creating a dielectric mirror. In general, a dielectric mirror's reflectance spectrum consists of *notches* of high reflectance surrounded by regions of low reflectance, which approximates an ideal notch reflector. However, it may also exhibit ripple, high order HR regions, and

roll-off, which may effect the system signal (Fig. 7b).

Two optical film designs are considered for the creation of notch reflectors: quarter wavelength dielectric stack (QWDS) films and rugate films. QWDS films are the most common way to create high reflectance films in specific parts of the spectrum and are used widely as optical coating. QWDS films consist of discrete alternating thin film layers of high and low index of refraction material. Rugate films are less common and have only recently come into commercial use. These films consist of a continuous or quasi-continuous variation, usually sinusoidal, between an index of refraction maximum and minimum. Although advanced optical film design can be used to help eliminate effects such as ripple (side-lobes) and HR roll-off (Southwell 1989, Young 1967), in the simplest case these effects are present.

The design of narrow high reflectance notch reflectors for the systems proposed here using these methods is explored in depth in Perez and Shkel (2004). There it was noted that both the notch width  $\Delta\lambda_R$  and notch reflectance  $R_{\max}$  are strongly dependent on the ratio of the thin film indexes of refraction,  $(\frac{n_H}{n_L})$ . For the creation of narrow notch high reflectors, the ratio of optical indexes is very low. For example, in the case of a system similar to that simulated in Fig. 7, the use of either technique requires  $\frac{n_H}{n_L} \approx 1.05$ . In the case of discrete optical films commonly used in QWDS reflectors, this ratio is rarely observed to be below  $\sim 1.5$  (Macleod 2001). It is expected that due to the continuous variation in optical index, the  $\frac{n_H}{n_L}$  of rugate films will not be similarly limited on the lower end. Also rugate films have design flexibility that leave them better suited for the close approximation of ideal notch reflectors (Bovard 1990). Due to this and the fact that spectral reflectance characteristics of a simple sinusoidal rugate film and of a simple QWDS film are similar, we consider the simulation of a serialized system of FPIs composed of rugate film reflectors.

Using the characteristic matrixes method, wherein the optical properties of each discrete layer are defined as a  $2 \times 2$  matrix and the product of these matrixes defines the optical properties of a composite structure (Nussbaum and Phillips 1976), the spectral reflectance curves of each designed structure was

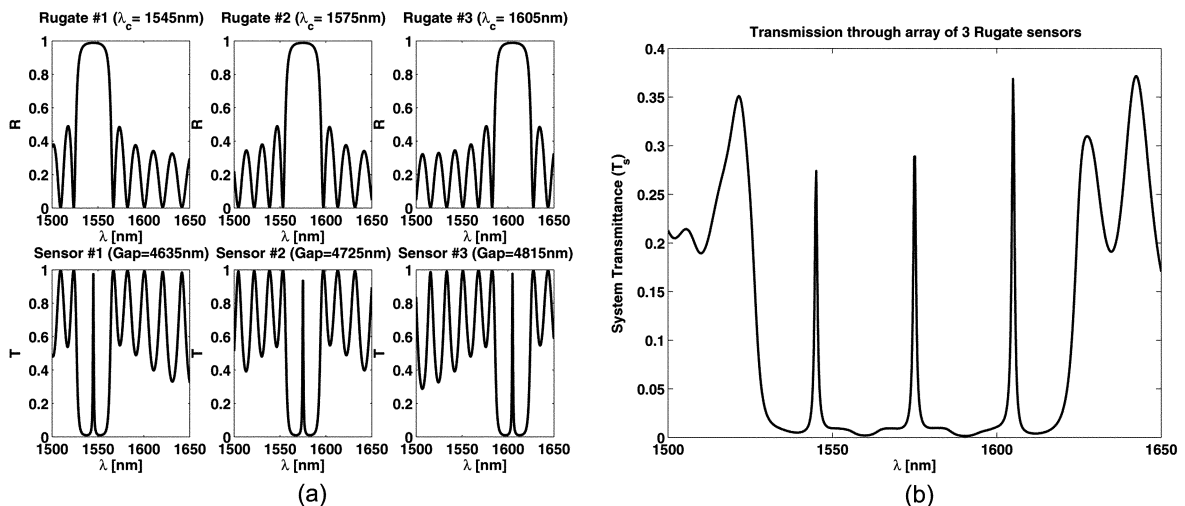


Fig. 10 Numerical simulation of a series array of three FPI sensors constructed of rugate optical films designed such that  $R_{\max}=0.97$ . (a) On the top, the individual reflectance characteristics, and the bottom, transmittance characteristics and (b) the system transmittance signal for  $n=6$

defined. For the simulation of a rugate film, the continuous film was approximated by twenty-five discrete layers for each optical index period and a matrix was defined for each layer. These reflectance curves could then be used with the Airy function to define the transmittance of each sensor and the serialized system in a manner identical to that of the ideal case.

We simulate a system designed to have notch characteristics identical ( $R_{\max}=0.97$ ,  $\Delta\lambda_R = 30$  nm) to the system shown in Fig. 8 to study the effects of ripple and roll-off characteristic of real high reflectors on serialized systems (Fig. 10). One should notice that the regions of ripple exhibit a reflectance that can be approximated by an effective  $R_{\text{pass}}$  of 0.3 resulting in the dramatic attenuation output fringes of over 60%. However, even in the presence of such a complex reflectance pattern, easily discernible fringes are evident in the output signal using the serialized notched FPI architecture since the attenuation envelope does not alter the individual Airy fringes significantly.

#### 4. Device fabrication and testing

In order to construct optical accelerometers with the serializable properties presented in section III-B, precision layers of optical thin films must be deposited on the inner plate surfaces of a mechanical system of the form of Fig. 2c. In addition, tight mechanical tolerances must be guaranteed in order to satisfy the requirements, presented in Section II-C, in order to achieve resolutions on the order of those calculated in Section II-D. Although a variety of integrated processes have been used over the past decade to create such devices, the precision processing required to create the optical thin films with narrow, highly-reflective, and precisely placed high-reflectivity spectral regions implies that these deposition processes be carried out by in dedicated facilities by those trained in the art. The goal then is to develop a fabrication process to create suspended elements of a substrate treated with such films and an assembly process to construct FPIs of such elements to the tolerances required by Fig. 4. For the resolutions calculated in section II-D, these processes must produce devices with maximum deviations from ideal at the level of a quarter nanometer.

It is initially assumed that optical thin film deposition is done on a double-sided finely polished silicon wafer (Fig. 11a-Step 1) such that the roughness is below of acceptable limits. Single crystal silicon is used as the structural material. For the wavelength of interest (1500 nm-1700 nm), the silicon

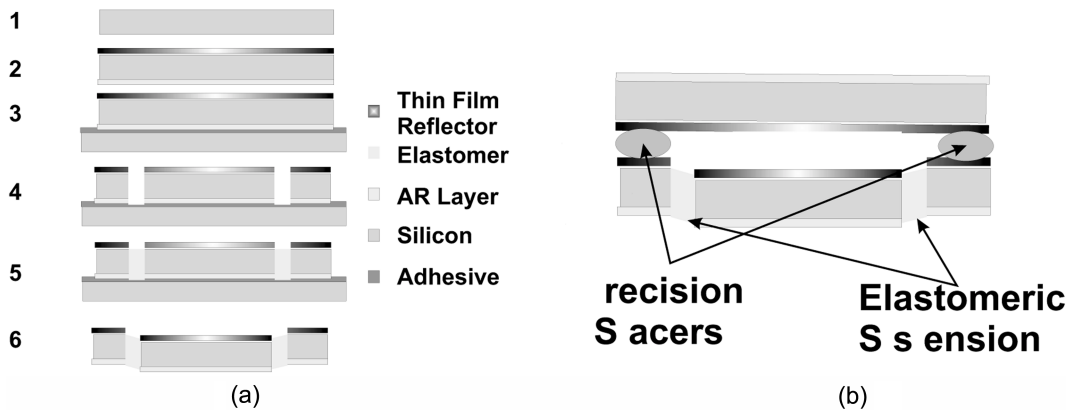


Fig. 11 (a) The fabrication process developed to take advantage of high precision optical thin film deposition and (b) an assembled device using such a process

is transparent, and thus a suitable choice. The thin film reflector is deposited on one-side and an anti-reflection layer is placed on the opposite side (Fig. 11a-Step 2) such that the expected residual stresses are balanced to prevent spherical bowing of the wafer. After being lithographically patterned with a closed, hollow shape such as a circle, the wafer is mounted on a handle wafer with a thin layer of photoresist or some other vacuum acceptable adhesive (Fig. 11a-Step 3). A deep reactive ion etching (DRIE) system is used to through-etch the wafer according to the patterning creating a trench to the handle wafer (Fig. 11a-Step 4). This trench is then back-filled with a liquid polymer such as polydimethylsiloxane (PDMS) (Fig. 11a-Step 5). This step needs to be done very carefully not to contaminate the optical surface. This polymer is then cured to create an elastic suspension and the handle wafer is removed (Fig. 11a-Step 5), leaving the center section defined by the trench free to respond to accelerations in the out-of-plane direction.

The outer 'frame' of the suspended reflective element can be fixed relative to a non-suspended reflective element via a stable epoxy to create the 'at-rest' spacing between the plates (Fig. 11b). The plates must be carefully aligned to the requisite parallelism tolerances. For this, a three degree-of-freedom (pitch, roll,  $z$  displacement) alignment stage is used before the spacer is set. During alignment, a broadband light source is transmitted through the FPI and the transmitted fringe is monitored on an OSA. The best possible alignment occurs when the narrowest fringe is detected.

Several fabrication approaches were explored to evaluate the fabrication process and test the properties of elastomer mechanical suspensions. The first approach was to consider AZ 4620 photoresist, Crystalbond 509, and HeatSink Grease as an adhesive, (Fig. 11a-Step 4). The second approach was to slightly underetch silicon, leaving 10-20  $\mu\text{m}$  of silicon holding the frame to the suspended platform. Once the elastomer suspension was deposited and cured, this excess silicon was removed via mechanical polishing. A sample created with this process is shown in Fig. 13a.

Fabricated devices were experimentally characterized. The frequency response of the plates suspended with the above fabrication methods were tested. Using an electrodynamic shaker (VTS 100) a sample was excited in the direction perpendicular to the chip and the laser doppler vibrometer (MetroLaser VibroMet 500) was used to measure the response of the suspended plate. Fig. 13b shows the acceleration frequency response of a sample set of these devices with circular geometries of a variety of sizes. The principle mode of vibration is obvious in both the amplitude (peak response) and phase response ( $\pi/2$  crossover) plots. Preliminary FEA studies show that the principle mechanical mode is the expected out-of-plane deflection of the suspended platform and that the second mode is a trunion or torsional mode (Fig. 12). This second mode is detrimental to the resolution of the device (non-parallel motion). The FEA studies indicate that the second mode is generally  $\sim 1.5$  times higher than the first mode for this suspension type for a wide range of geometries. Due to this one would expect to pick up a strong response in the 500-800 Hz region due to trunion motion. However, none is observed. This indicates substantial decoupling between

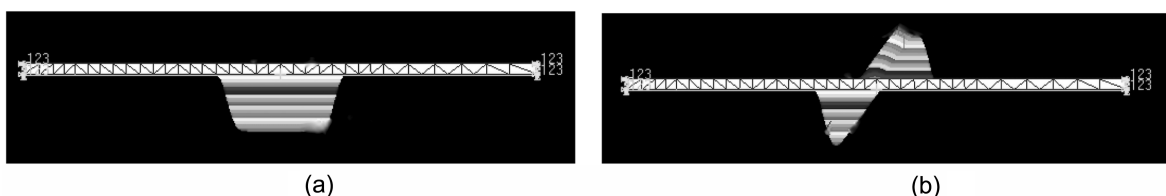


Fig. 12 FEA results demonstrating the (a) first mode out-of-plane deflection and (b) the second mode trunion deflection of an elastomer suspended plate under inertial excitation.

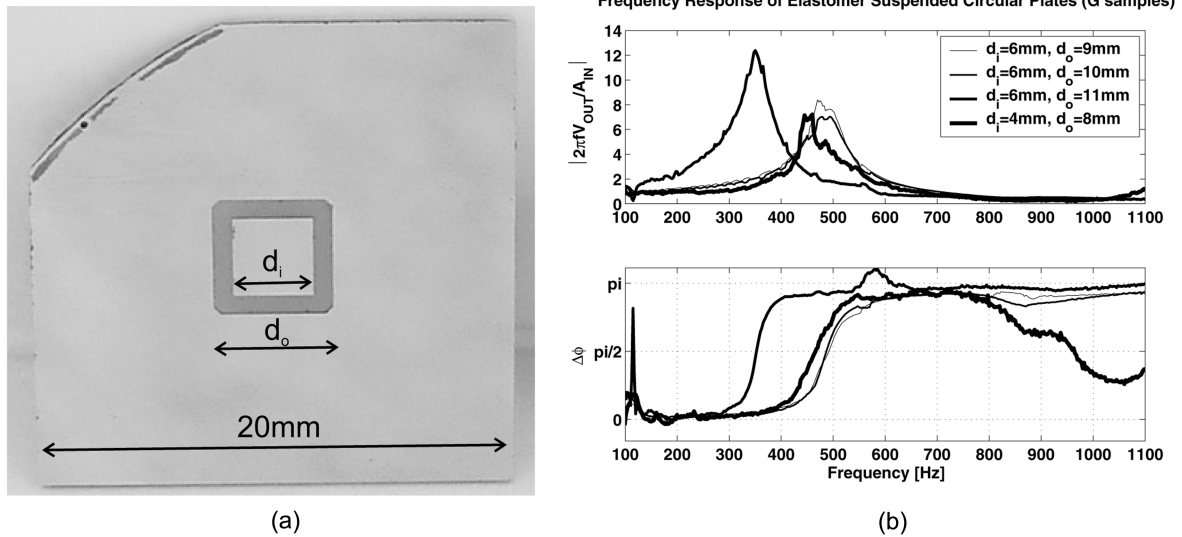


Fig. 13 (a) A suspended silicon platform with a PDMS (Silgard 182) elastomer suspension and (b) The mechanical frequency response of a set of such devices (outer diameter  $d_o$ , inner diameter  $d_i$ ) excited with out-of-plane sinusoidal  $\pm 2$  g acceleration at the outer frame.

these two modes as no out-of-plane excitation was detected in coupling to the detrimental trunion mode for this fabrication technique. The experimental results demonstrate manufacturability of optical accelerometers utilizing polymer as a mechanical suspension.

## 5. Conclusions

A network of optical inertial sensors based on suspended Fabry-Perot cavities is proposed for use on highly sensitive and/or widely distributed structures. The properties of the sensor class was described and the mechanical and optical properties are incorporated into a set of relations describing the sensor characteristics. Using these relations, sub- $\mu\text{g}$  acceleration resolutions were estimated for high optical resolution devices. Using the properties of optical thin films to create intrinsic wavelength division of the sensor signals, a method of serialization was developed for such devices. The properties and drawbacks of such a system were carefully studied and practical guidelines for implementation are presented. A fabrication process was developed to allow the construction of such devices from substrates coated with the required precision optical films. Test structures were fabricated from this process and dynamic vibration tests are performed. Our findings confirm that the combination of optical detection, utilization of high compliance materials, and linear serialization of sensors will result in devices capable to detect vary small amplitude ambient vibrations in a very broad frequency range.

## Acknowledgements

Authors would like to acknowledge Mr. Michael Little, Augura Technologies Inc., for useful and motivating discussions. This work is supported by the National Science Foundation Grant CMS-

0330470, program director Dr. Shih-Chi Liu.

## References

- Aktan, A., Tsikos, C. J., Catbas, F. N., Grimmelsman, K. and Barrish, R. (1999), "Challenges and opportunities in bridge health monitoring", *Proceedings of the Second International Workshop on Structural Health Monitoring*, Edited by F.-K. Chang.
- Atherton, P. D., Reay, N. K., Ring, J. and Hicks, T. R. (1981), "Tunable fabry-perot filters", *Optical Engineering* **20**(6), 806-814.
- Bartek, M., Correia, J. H. and Wolffenbuttel, R. F. (1999), "Silver-based reflective coatings for micromachined optical filters", *J. Micromechanics and Microengineering* **9**(2), 162-165.
- Born, M. and Wolf, E. (1999), *Principles of Optics* (7th ed.). Pergamon, London.
- Bovard, B. G. (1990, January), "Rugate filter design: the modified fourier transform", *Applied Optics*, **29**(1), 24-30.
- Choqueta, P. and Juneau, F. (2000), "New generation of fabry-perot fiber optic sensors for monitoring of structures", *Proceedings of SPIE's 7th Annual International Symposium on Smart Structures and Materials*.
- Chong, K. P. (1997), "Health monitoring of civil infrastructures", *Proceedings of the Second International Workshop on Structural Health Monitoring*, Edited by F.-K. Chang.
- Cooper, E. B. and Post, E. R. (2000), "High-resolution micromachined interferometric accelerometer", *Applied Physics Letters*, **76**(22), 3316-3318.
- Cristea, D., Kusko, M., Tibeica, C., Muller, R., Manea, E. and Syvridis, D. (2004), "Design and experiments for tunable optical sensor fabrication using (111)-oriented silicon micromachining", *Sensors and Actuators A-Physical*, **113**(3), 312-318.
- Fabry, C. and Perot, A. (1899), "Théorie et applications d'une nouvelle méthode de spectroscopie interférentielle", *Ann. Chim Phys. Paris* **16**, 115-144.
- Gerges, A. S. and Newson, T. P. (1989a), "High-sensitivity fiber-optic accelerometer", *Optics Letters*, **14**(4), 251-253.
- Gerges, A. S. and Newson, T. P. (1989b), "Practical fiber-optic-based submicro-g accelerometer free from source and environmental perturbations", *Optics Letters* **14**(20), 1155-1157.
- Goff, D. R. (1999). *Fiber Optic Reference Guide*, Focal Press-Boston.
- Kartalopoulos, S. V. (2000). *Introduction to DWDM Technology: Data in a Rainbow*. IEEE Press, New York.
- Macleod, H. A. (2001), *Thin-Film Optical Filters* (3ed.). Institute of Physics Publishing, Bristol-Philadelphia.
- Nussbaum, A. and Phillips, R. A. (1976), *Contemporary Optics for Scientists and Engineers*. Prentice-Hall, Inc.
- Patterson, J. D. (1997, September), *Micro-Mechanical Voltage Tunable Fabry-Perot Filters Formed in (111) Silicon*. Phd, University of Colorado, Boulder.
- Perez, M. A. and Shkel, A. M. (2004), "On serializing fabry-perot micro-accelerometers", *The 1st International Workshop on Advanced Smart Materials and Smart Structures Technology*, pp. 276-283.
- Raley, N. F., Ciarlo, D., Koo, J. C., Trujillo, J., Yu, C., Loomis, G. and Chow, R. (1992), "A fabry-perot microinterferometer for visible wavelengths", *IEEE Solid-State Sensor and Actuator Workshop, 5th Technical Digest*, 170-173.
- Solus-Micro-Technologies (2002), "New tunable filters use compliant mems technology to deliver superior performance at lower cost in optical networking applications", Internet Press Release. URL: [http://www.solustech.com/news\\_events/press\\_room/Mar\\_11\\_02.htm](http://www.solustech.com/news_events/press_room/Mar_11_02.htm).
- Southwell, W. H. (1989), "Using apodization functions to reduce sidelobes in rugate filters", *Applied Optics*, **28**(23), 5091-5094.
- Stephensa, M. (1993), "A sensitive interferometric accelerometer", *Rev. Sci. Instrum.* **64**(9), 2612-2614.
- Todd, M., Johnson, G., Vohra, S. T., Chen-Chang, C., Danver, B. and Malsawma, L. (1999), "Civil infrastructure monitoring with fiber bragg grating sensor arrays", *Proceedings of the Second International Workshop on Structural Health Monitoring*, Edited by F.-K. Chang.
- Udd, E. (1990). *Fiber Optic Sensors*. John Wiley and Sons, Inc.
- Vohra, S. T., Danver, B., Tveten, A. and Dandridge, A. (1997), "High performance fiber optic accelerometers", *Electronics Letters* **33**(2), 155-157.

- Waters, R. L. and Aklufi, M. E. (2002, October), "Micromachined fabry-perot interferometer for motion detection", *Applied Physics Letters*, **81**(18), 3320-3322.
- Winchester, K. J. and Dell, J. M. (2001, September), "Tunable fabry-perot cavities fabricated from pecvd silicon nitride employing zinc sulphide as the sacrificial layer", *J. Micromechanics and Microengineering* **11**(5), 589-594.
- Yamakawa, H., Iwaki, H., Mita, A. and Takeda, N. (1999), "Health monitoring of steel structures using fiber bragg grating sensors", *Proceedings of the Second International Workshop on Structural Health Monitoring*, Edited by F.-K. Chang.
- Young, L. (1967), "Multilayer interference filters with narrow stop bands", *Applied Optics* **6**(2), 297-315.

CC